SCIENCE CHINA
Chemistry

•ARTICLES•

April 2021 Vol.64 No.4: 565–575
https://doi.org/10.1007/s11426-020-9917-6

Single-wall carbon nanotube-containing cathode interfacial materials for high performance organic solar cells

Fei Pan[1,2,5†], Song Bai[1†], Tianhao Liu[1,6], Dianyong Tang[3], Xian Wei[1], Xiwen Chen[4], Menglan Lv[1,2,6*] & Yongfang Li[2,5*]

[1]*School of Chemical Engineering, Guizhou Institute of Technology, Guiyang 550003, China;*
[2]*Beijing National Laboratory for Molecular Sciences, CAS Key Laboratory of Organic Solids, Institute of Chemistry, Chinese Academy of Sciences, Beijing 100190, China;*
[3]*Chongqing Engineering Laboratory of Targeted and Innovative Therapeutics, International Academy of Targeted Therapeutics and Innovation, Chongqing University of Arts and Sciences, Chongqing 402160, China;*
[4]*Guangzhou Polyforte Chemical Technology Co. LTD, Guangzhou 510520, China;*
[5]*School of Chemical Science, University of Chinese Academy of Sciences, Beijing 100049, China;*
[6]*School of Chemistry and Chemical Engineering, Guizhou University, Guiyang 550025, China*

Received September 23, 2020; accepted December 4, 2020; published online February 22, 2021

Water/alcohol soluble cathode interfacial materials (CIMs) are playing important roles in optoelectronic devices such as organic light emitting diodes, perovskite solar cells and organic solar cells (OSCs). Herein, *n*-doped solution-processable single-wall carbon nanotubes (SWCNTs)-containing CIMs for OSCs are developed by dispersing SWCNTs to the typical CIMs perylene diimide (PDI) derivatives PDIN and PDINO. The Raman and X-ray photoelectron spectroscopy (XPS) measurement results illustrate the *n*-doped behavior of SWCNTs by PDIN/PDINO in the blend CIMs. The blended and *n*-doped SWCNTs can tune the work function and enhance the conductivity of the PDI-derivative/SWCNT (PDI-CNT) composite CIMs, and the composite CIMs can regulate and down-shift the work function of cathode, reduce the charge recombination, improve the charge extraction rate and enhance photovoltaic performance of the OSCs. High power conversion efficiency (PCE) of 17.1% and 17.7% are obtained for the OSCs based on PM6:Y6 and ternary PM6:Y6:$PC_{71}BM$ respectively with the PDI-CNT composites CIMs. These results indicate that the *n*-doped SWCNT-containing composites, like other *n*-doped nanomaterials such as zero dimensional fullerenes and two dimensional graphenes, are excellent CIMs for OSCs and could find potential applications in other optoelectronic devices.

organic solar cells, cathode interfacial materials, *n*-doped single wall carbon nanotubes, silver electrode

Citation: Pan F, Bai S, Liu T, Tang D, Wei X, Chen X, Lv M, Li Y. Single-wall carbon nanotube-containing cathode interfacial materials for high performance organic solar cells. *Sci China Chem*, 2021, 64: 565–575, https://doi.org/10.1007/s11426-020-9917-6

1 Introduction

Organic solar cells (OSCs) using bulk heterojunctions (BHJ) active layer of *p*-type conjugated polymer donor and *n*-type non-fullerene acceptor have been widely studied due to their unique merits of mechanical flexibility, light weight and low-cost solution-printable preparation technology [1–14]. Lately, the power conversion efficiencies (PCEs) of OSCs have been improved dramatically to 15%–17% for the single junction OSCs *via* employing the low bandgap *n*-type organic semiconductor (such as Y6) as acceptor [3,4] and wide bandgap conjugated polymer as donor [2,3,5,6].

In addition to developing the high-performance photovoltaic materials, it is also crucial to develop high performance electrode interfacial materials for realizing

†These authors contributed equally to this work.
*Corresponding authors (email: lvmenglan@git.edu.cn; liyf@iccas.ac.cn)

industrialization of the OSCs. Good electrode interfacial materials need to possess suitable work function, high charge carrier mobility and high conductivity [7–10]. Water/alcohol soluble cathode interfacial materials (CIMs) are playing important roles in optoelectronic devices such as organic light emitting diodes, perovskite solar cells and OSCs, as they can provide solution processability, reduce cathode work function, suppress charge recombination *etc*. [11–14]. In recent years, the CIMs are developed from neutral to *n*-doped materials with high conductivity due to their *n*-type nature. The *n*-doped materials include *n*-doped polymers, *n*-doped organic small molecules, and *n*-doped fullerene derivatives [15–21]. Very recently we introduced *n*-doped graphene-containing CIMs in OSCs [22]. The graphenes dispersed in a classical alcohol soluble electron transport material (*N*,*N*-dimethyl-ammonium N-oxide) propyl perylene diimide (PDINO) could provide a power conversion efficiency of 16.52% for OSCs based on PM6:Y6 [22,23]. Single-wall carbon nanotube (SWCNT) could be considered as a rolled-up graphene sheet, and was used as an anode interfacial material as graphene did before and little has been tried as cathode interfacial materials due to its high work function [24,25]. Similar to graphene, it may be doped by the PDINO CIM to form the high performance composite CIMs of PDINO and SWCNT. In addition, SWCNT also possesses unique properties such as excellent charge carrier mobility, higher conductivity, good transparency, flexibility, and solution processing compatibility. Several *n*-doping methods have been developed for carbon nanotubes (CNTs), such as gaseous molecules filling, vacuum or inert gas annealing, inorganic materials intercalation, electrochemical reduction, organic materials adsorption [26–29]. In this work, we apply the strategy of dispersing CNTs in traditional water-alcohol soluble PDI derivatives CIMs (*N*,*N*-dimethylamino)propyl perylene diimide (PDIN) and PDINO [29], and high PCEs of 17.1% and 17.7% are obtained for the OSCs based on PM6:Y6 and PM6:Y6:$PC_{71}BM$ active layers, respectively, benefitted from the excellent cathode interfacial properties of the SWCNT-containing composite CIMs. It should be mentioned that the PDI-derivatives have a large planar electron-deficient π-system to interact with CNT *via* π-π interactions, hydrophobic forces, and Coulombic attraction for dispersion, and show good doping effect. In addition, the PDI-derivatives have suitable molecular diameters (about 10 Å), which could exist both inside and outside the SWCNTs. Therefore, we select the PDI-derivatives to blend with SWCNT for the composite CIMs.

2 Experimental

2.1 Materials and methods

Graphene oxide (GO, length: 0.5–5.0 mm; layer thickness: 0.335–1.0 nm; layer number: 1; and purity: 99.9%), commercial semi-open single-walled carbon nanotube (SWCNT, preparation: chemical vapor deposition method; purity >97 wt%; external diameter ≤2 nm; length: 5–30 μm; conductivity 100 S cm^{-1}) and SWCNT films were purchased from Suzhou Tanfeng Graphene Technology Co. Ltd. PM6, Y6, PDINO and PDIN were purchased from Solarmer Materials Inc. and used as received without further purification. Other chemicals and solvents were obtained from Alfa Aesar Chemical. Co. Poly(3,4-ethylenedioxythiophene):polystyrene sulfonate (PEDOT:PSS, PVP Al 4083) was obtained from H. C. Starck. The ITO glass (thickness 135 nm, ≤15 Ω per square, transmittance ≥86%, soda-lime glass and Nippon sheet glass) was purchased from South China Science & Technology Company, Ltd. The carbon nanotube composite cathode interfacial materials (CIMs) were made by dispersing the carbon nanotubes in the surfactants in ethanol with ultrasonication for 60 min in an ice-water bath.

2.2 Device fabrication and characterization

The architecture of devices were high transmittance indium tin oxide (ITO)/GO/PEDOT:PSS/active layer/CIMs/Al (or Ag). Pre-cleaned ITO substrates were treated by UV-ozone treatment for 30 min, and then 8 nm GO (from 0.3 mg mL^{-1} aqueous solution) was coated onto the ITO. After that, about 30 nm PEDOT:PSS was coated onto the ITO/GO substrates, and dried at 150 °C for 30 min in air. Then the treated substrates were transferred to a glove box with nitrogen-protection. PM6:Y6 (1:1.2 weight ratio) and PM6:Y6:PC_{71}BM (1:1.2:0.2 weight ratio) in chloroform:chloronaphthalene (99.5:0.5 volume ratio) solution were spin-coated onto the GO/PEDOT:PSS substrates to obtain a film thickness of approximately 100 nm. The active layers were annealed at 110 °C for 10 min for the PM6:Y6 binary blends and at 90 °C for 10 min for the PM6:Y6:PC_{71}BM ternary blends, respectively. Then ethanol solution of SWCNT composite CIM at PDIN (with 0.3% CH_3COOH) or PDINO concentration of 1.5 mg mL^{-1} with 3% CNT was deposited on the active layer at 3,000 r min^{-1} to give a thickness of 10 nm (unless otherwise stated). Finally, 100 nm of aluminum or silver was thermally deposited atop the interface in a vacuum chamber at a pressure of about 5.0×10^{-5} Pa. A shadow mask with an effective device area of 0.046 cm^2 was used.

The current density-voltage (*J*-*V*) characteristics were measured using a computer-controlled Keithley 2400 source measurement unit under 1 sun, AM 1.5 G spectrum from a classic solar simulator (Newport 94023A) with a 450 W xenon lamp in a glove box filled with nitrogen (O_2<0.1 ppm, H_2O<0.1 ppm). The light intensity was calibrated to be 100 mW cm^{-2} by a Newport Oriel 91150V reference cell. The PCE results in this work are obtained using more than 15 individual devices fabricated under the same conditions. The

EQE was measured using a Solar Cell Spectral Response Measurement System QE-R3-011 (Enli Technology Co. Ltd.). The light intensity at each wavelength was calibrated with a standard single-crystal Si photovoltaic cell.

2.3 Instruments and measurements

The bath ultrasonicator was purchased from Shenzhen Pinhuang Science and Technology Ltd. (Model Number: Dongsen DS-040ST) with the ultrasonic maximum power of 240 W, ultrasonic frequency 40 kHz, and max capacity 10 L. Scanning Kelvin probe microscopy was implemented on a KP Technology SKP5050. X-ray photoelectron spectroscopy (XPS) measurements were performed on an ESCALab220i-XL system. Raman spectra were recorded using an Olympus FV1000-IX81 Raman microscope equipped with a 533 nm/632 nm Ar ion laser. Transmission electron microscopy (TEM) measurements were performed on a JEOL JEM-2100 system (Japan). Scanning electron microscopy (SEM) measurements were performed on a Zeiss Sigma 500 (UK).

Transient photocurrent (TPC) measurements: the transient photocurrent response of the devices was taken at short circuit condition to a 200 μs square pulse from the LED with no background illumination. The current traces were recorded on an Ektronix DPO3034 digital oscilloscope by measuring the voltage drop over a 5 ohm sensor resistor in series with the solar cell. DC voltage was applied to the solar cell with an MRF544 bipolar junction transistor in common collector amplifier configuration.

Transient photovoltage (TPV) measurements: in the TPV measurements, a 405 nm laser diode was used to keep the organic solar cells in the V_{oc} conditions. Measuring the light intensity with a highly linear photodiode and driving the laser intensity with a waveform generator (Agilent 33500B, USA) allowed reproducible adjustments of the light intensities under one sun. Moreover, a small perturbation was induced with a second 405 nm laser diode. The intensity of the short laser pulse was adjusted to keep the voltage perturbation below 10 mV. After the pulse, the voltage decays back to its steady state value in a single exponential decay.

Prior to analysis, the CNTs were dispersed in ethanol after sonication for 2 min and then drop-casted onto a Cu TEM grid covered with a thin amorphous carbon film. The SEM samples were prepared by dispersing the CNTs in ethanol after sonication for 2 min. The Raman samples of SWCNT composites were prepared by vacuum filtration of PDIN-CNT and PDINO-CNT dispersion (centrifuged at 5,000 r min^{-1} for 30 min) with a polyvinylidene fluoride membrane (pore size: 0.45 mm), followed by careful washing with deionized water, methanol and ethanol once to remove the free surfactants, and drying under vacuum for 3 h. Raman samples of CNT films were prepared by soaking in the solutions of PDIN or PDINO for 2 h, followed by careful washing with ethanol once to remove the redundant surfactant, and drying under vacuum for 3 h. The XPS and scanning Kelvin probe microscopy (SKPM) samples of PDIN-CNT and PDINO-CNT were prepared by spin-coating the PDIN-CNT and PDINO-CNT dispersion (2 mg mL^{-1} PDINO (or PDIN) solution with different ratio of CNT) at 1,000 r min^{-1} for 30 s onto silicon dioxide substrates (for XPS), ITO and evaporated Ag substrates (for SKPM), respectively.

3 Results and discussion

3.1 CNTs dispersibility characterization

Firstly, we select the typical CIMs PDI derivatives for the dispersion of SWCNT, considering that the large planar electron-deficient π-systems of PDI would interact with the CNTs *via* π-π interactions, hydrophobic forces, and Coulombic attraction for dispersion. As shown in Figures S1 and S2 (Supporting Information online), the diameter of pristine SWCNTs is about 19.3±1.8 Å, which is obtained by SEM and TEM observations. The calculated molecular diameters of the PDI derivatives are about 10 Å, which indicates that the PDI derivatives could exist both inside and outside the SWCNTs. The adsorption energies of PDI derivatives (PDIN and PDINO) on both inside and outside of the SWCNTs are calculated *via* periodic density functional theory (the simulation method described in supporting information) [30–32]. The calculated results suggest that they have large adsorption energies (Figures S3–S6 and Table S1, Supporting Information online). Thus both PDIN and PDINO are potentially good dispersants for SWCNT. In order to measure the SWCNTs dispersibility in different dispersants, the ice-bath ultrasonic was used to disperse the commercial SWCNT powder in ethanol. The quality of the commercial SWCNT was identified by XPS, SEM, TEM and Raman spectroscopy [26–28]. Figure S7 presents representative XPS C 1s spectrum for the SWCNT powder. The peak position at 284.4 eV is very close to the value (284.3 eV) for pure sp^2 C–C bonding in pristine highly oriented pyrolytic graphite [26–28], indicating carbon atoms are almost exclusively sp^2 hybridized in commercial SWCNTs. The SEM and TEM images of the CNT flakes indicated that mainly the single-walled CNTs.

Figure S8(a) shows the Raman spectra of the SWCNTs dispersed by a typical surfactant polyvinyl pyrrolidone (PVP) with excitation at 633 nm. Two maxima are apparent near 1,592 (G band) and 2,634 cm^{-1} (2D band). The narrow G band indicates that SWCNTs are semiconducting SWCNTs [32]. For the PDI derivative dispersants with SWCNT composites, two maxima are apparent near 1,586 (G band) and 2,623 cm^{-1} (2D band) for PDIN composite and 1,584 (G band) and 2,624 cm^{-1} (2D band) for PDINO

composite in the Raman spectra (Figure S8(b, c)). Meanwhile, the typical dispersions of the CNTs dispersibility in PDIN and PDINO CIMs are represented by the Tyndall effect, as shown in Figure S9. More detailed properties of these composite dispersion systems will be discussed below.

3.2 Photovoltaic properties

Afterwards, we investigated the potential of the SWCNT composite materials as CIMs in OSCs. SWCNTs were dispersed in two typical CIMs PDINO and PDIN (Hereinafter referred to as PDINO-CNT and PDIN-CNT, respectively) to form composite CIMs for OSCs. The graphene oxide (GO)/PEDOT:PSS composite was employed as the hole transport material [33–35]. We fabricated the traditional structure OSCs (ITO/GO/PEDOT:PSS/PM6:Y6/CIM/Al) using copolymer PM6 [36] as the electron donor and small molecule *n*-type organic acceptor Y6 [3] as the acceptor. Firstly, we optimized the SWCNT ratio in the composite CIMs by studying the effect of the SWCNT ratio from 1% to 10% on the photovoltaic performance of the OSCs with the composite CIMs, and the results are listed in Tables S4 and S5. It can be seen that the optimized SWCNT weight ratio is 3% for both PDINO and PDIN CIMs. Therefore, we use 3% SWCNT in the PDINO-CNT and PDIN-CNT CIMs in the following.

Figure 1 shows the chemical structures and energy level diagram of related materials studied in this work, schematic diagram of the OSCs and constructed model of PDI-CNT composite materials. Figure 2(a) and Table 1 display characteristic *J-V* curves and the photovoltaic data of the OSCs. The control devices with bare Al as the cathode exhibited the poorest device performance of 15.12% PCE with a short-circuit current density (J_{sc}) of 25.81 mA cm^{-2}, an open-circuit voltage (V_{oc}) of 0.847 V, and a fill factor (FF) of 69.15%. When the typical PDINO and PDIN CIMs were incorporated, the resulting devices delivered an enhanced PCE of 16.45% (V_{oc}=0.856 V, J_{sc}=26.01 mA cm^{-2} and FF=73.89%) and 16.49% (V_{oc}=0.854 V, J_{sc}=25.95 mA cm^{-2} and FF=74.44%), respectively. When PDINO-CNT and PDIN-CNT were used as the CIMs, the PCE increased to 17.12% (V_{oc}=0.855 V, J_{sc}=26.74 mA cm^{-2} and FF=74.87%) and 17.03% (V_{oc}=0.859 V, J_{sc}=26.43 mA cm^{-2} and FF=75.00%), respectively. The PCEs of the OSCs based on the CNT-containing CIMs are higher than that of the devices based on the graphene-containing analogue PDINO-G CIM as reported previously [22]. Figure 2(b) presents the external quantum efficiency (EQE) spectra of the PM6:Y6 OSCs with various CIMs. The integral current density values ($J_{calc.}$) calculated from the EQE spectra match well with the J_{sc} values from the *J-V* curves, with mismatch of less than 3% (Table 1).

3.3 SWCNTs composite CIMs characterization

In order to understand the device working mechanism of the SWCNTs composite CIMs for boosting photovoltaic performance of the OSCs, the conductivity and work function variation trends were measured. Two-point probe devices were fabricated using organic ribbon mask technique to measure the conductivities of CIMs, which were extracted from the experimental data in the region of the Ohmic contact [37]. All devices were measured in air at room temperature. Figure S10(a, b) show the two-point probe (without gate) *J-V* curves for the PDINO-CNT and PDIN-CNT CIMs with different CNTs ratio. The results display that the conductivity increased from 9.84×10^{-6} S cm^{-1} for PDINO to 2.07×10^{-2} S cm^{-1} for the composite CIM with 3% SWCNTs

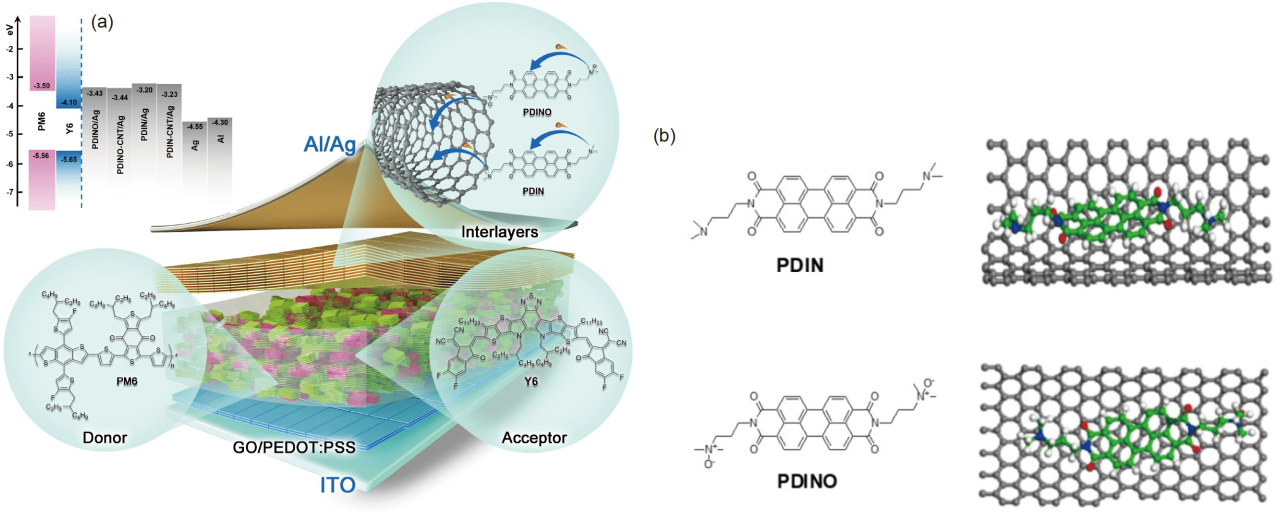

Figure 1 (a) Molecular structures of the photovoltaic and interfacial materials used in this work and schematic diagram of the OSCs; (b) the constructed model of PDIN/SWCNT and PDINO/SWCNT (inside) (color online).

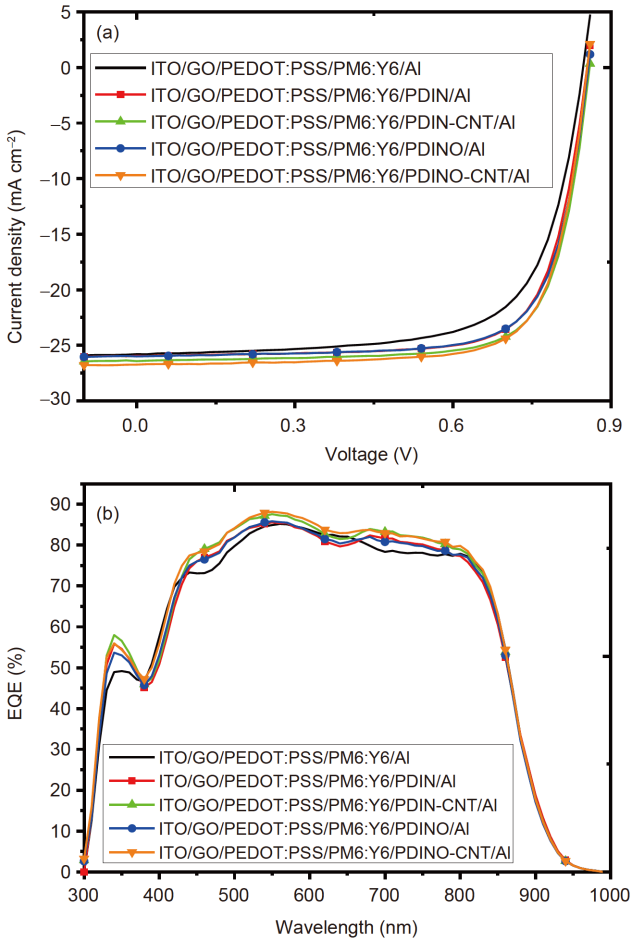

Figure 2 Photovoltaic performance of the OSCs based on PM6:Y6 with Al electrode. (a) *J*-*V* curves of the OSCs with different CIMs under the illumination of AM 1.5 G, 100 mW cm^{-2}; (b) external quantum efficiency spectra of the corresponding OSCs (color online).

in PDINO, and from 6.47×10^{-6} S cm^{-1} for PDIN to 9.89×10^{-3} S cm^{-1} for the composite CIM with 3% CNTs in PDIN, both increased by over 3 orders of magnitude. We also measured conductivities of the different CIMs using the space-charge limited current (SCLC) method [38] with the device structure of ITO/PDINO-CNT (or PDIN-CNT)/Al as shown in Figure S10(c, d) and Table S2. A similar trend emerged with the two-point probe method. The conductivities of the composite PDINO-CNT (2.07×10^{-2} S cm^{-1}) and PDIN-CNT (9.89×10^{-3} S cm^{-1}) CIMs are higher than that (1.18×10^{-3}–4.25×10^{-3} S cm^{-1}) of PDINO-G [22], which may be one of the reasons why they work better than PDINO-G CIM in the OSCs.

Meanwhile, SKPM was used to measure the variation trend of work function on various electrode surfaces treated by different CIMs. The work function data of the CNTs composites with different SWCNTs doping ratios on ITO and evaporated silver (Ag) electrode substrates are shown in Table S3. The work function of ITO electrode was set at 4.70 eV, and evaporated Ag electrode conducts reasonable work functions of 4.55±0.03 eV which are used as the references [39–41]. After PDINO solution treatment, the work functions were reduced to 3.97 eV for ITO substrate and 3.43 eV for evaporated Ag. The CNTs composite PDINO-CNT with different SWCNTs ratio reduced the work function by 0.71–1.11 eV on the evaporated Ag electrode and by about 0.7 eV on ITO electrode. All the work function values are lower than that of CNTs electrode (4.70 eV) obviously [42,43], which confirm that the nanotubes composite enhanced the cathode interfacial modification property with rational work functions.

Raman spectra were used further to explore the electronic states of the SWCNTs containing materials (Figure 3(a, b) [26–28,44–48]. The Raman spectrum of SWCNTs dispersed in a classical dispersant PVP showed a G band at 1,592 cm^{-1} and the 2D band at 2,634 cm^{-1}. Both were red-shifted by 8 and 10 cm^{-1}, respectively, for the SWCNTs dispersed in PDINO. In comparison, the SWCNTs film covered with PDINO displayed a red shifted G band and 2D band by 2 and 4 cm^{-1}, respectively. The larger red-shifts for the SWCNTs dispersed in PDINO relative to the SWCNT film covered with PDINO could indicate different electronic states of SWCNTs in the dispersed composite and in the SWCNT films [26–28,44–48]. In dispersed composite, SWCNTs could interact with the PDINO dispersant both on its surface and within the tubes while as a film it can only interact with PDINO on its surface. Theoretical calculation confirmed that the absorption energy of PDINO on the inner tube (−2.34 eV) is larger than that on the outer tube (−1.48 eV). Thus the stronger interaction between SWCNT and PDINO in the composite could result in the larger red-shifts. PDIN showed similar Raman behavior as PDINO. The large red-shift of both G and 2D bands could indicate moderate degree

Table 1 Photovoltaic performance data of the OSCs based on PM6:Y6 with different CIMs/Al cathode under the illumination of AM 1.5 G, 100 mW cm^{-2}

Structure of OSCs	V_{oc} (V)	J_{sc} ($J_{calc.}$)[a] (mA cm^{-2})	FF (%)	PCE_{max} (PCE_{avg}) (%)
ITO/GO/PEDOT:PSS/BHJ/Al	0.847	25.81(25.09)	69.15	15.12(14.8±0.3)
ITO/GO/PEDOT:PSS/BHJ/PDIN/Al	0.854	25.95(25.23)	74.44	16.49(16.3±0.2)
ITO/GO/PEDOT:PSS/BHJ/PDIN-CNT/Al	0.859	26.43(25.77)	75.00	17.03(16.8±0.2)
ITO/GO/PEDOT:PSS/BHJ/PDINO/Al	0.856	26.01(25.28)	73.89	16.45(16.3±0.2)
ITO/GO/PEDOT:PSS/BHJ/PDINO-CNT/Al	0.855	26.74(25.96)	74.87	17.12(16.8±0.3)

a) The $J_{calc.}$ from the external quantum efficiency spectra.

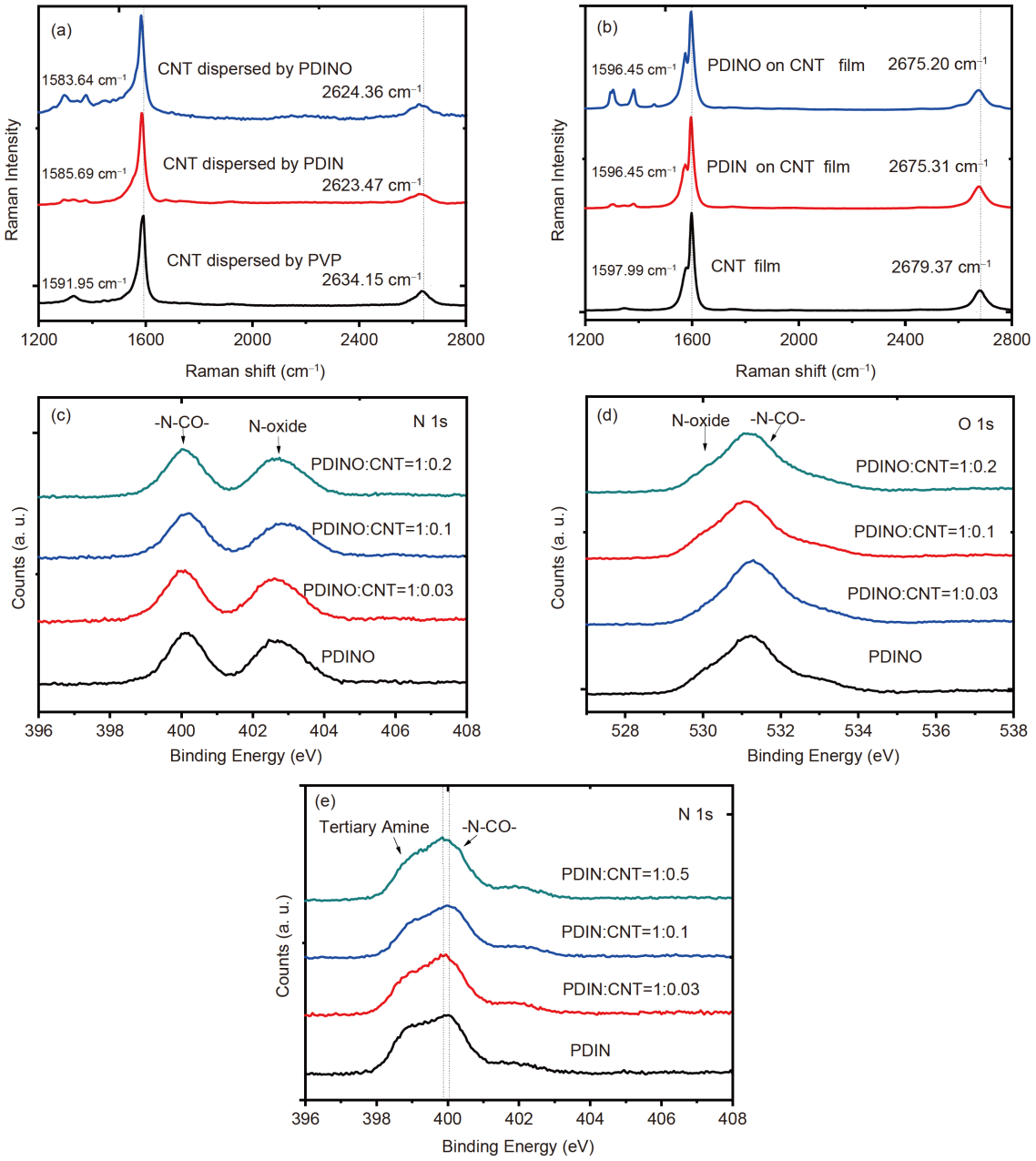

Figure 3 (a) Raman spectra for CNT dispersed in different dispersants; (b) Raman spectra for CNT film treated without and with PDIN and PDINO; (c) N 1s XPS spectra and (d) O 1s XPS spectra for PDINO and PDINO-CNT with different CNT ratios; (e) N 1s XPS spectra for PDIN and PDIN-CNT with different CNT ratios (color online).

of *n*-doping of the SWCNTs by both PDINO and PDIN, in agreement with other *n*-doping behaviors [44–48].

In addition, XPS was used to characterize the valence band changes and the elemental composition. The N 1s binding energy and the assignment of the PDINO-CNT are shown in Figure 3(c–e) and Table 2. For PDINO only, the N 1s at ~403 eV was assigned to free N-oxide while the broad peak at ~400 eV was assigned to both amide and the rest N-oxide which has donated electron to the perylene aromatic ring of PDINO [22]. Accordingly, the O 1s binding energy at ~530 eV is assigned to the free N-oxide and that peak at ~531 eV to both amide and the N-oxide which has transferred electrons to the perylene aromatic ring. A self n-doping level around 1.5% could be estimated from the N 1s binding energy results (0.99% from O 1s). With the increase of the SWCNTs in the composites, the ratio of N 1s at ~400 eV to N 1s at 403 eV increased, indicating more *N*-oxides are involved in the electron transferring to SWCNT. For PDINO-CNT (1:0.03), 4.2% of the N-oxide involved in the electron transferring to either perylene or SWCNTs. For PDIN-CNT composites, N 1s at 399 eV is assigned to the free amine and that at ~400 eV to both the

Table 2 The N and O quantification of PDINO-CNT and PDIN-CNT with different SWCNT ratio by XPS

	The ratio of N 1s (403 eV) /N 1s (400 eV)	The ratio of O 1s (531 eV) /O 1s (530 eV)		The ratio of N 1s (400 eV)/ N 1s (399 eV)
PDINO	0.97	2.03	PDIN	1.27
PDINO:CNT=1:0.03	0.92	2.92	PDIN:CNT=1:0.03	1.32
PDINO:CNT=1:0.10	0.88	3.90	PDIN:CNT=1:0.10	1.39
PDINO:CNT=1:0.20	0.88	4.42	PDIN:CNT=1:0.20	1.34

amide and the amine which has transferred electron to perylene ring or to the SWCNTs. A self *n*-doping level of 12% is thus estimated for PDIN. For PDIN:CNT(1:0.03), 14% of the amine involved in the electron transferring. Thus the *n*-doping level for PDIN-CNT is relatively higher than that for PDINO-CNT [26,27,45–49].

In order to further study the morphology change with different CIMs treatment, AFM and SEM measurements were performed, and the results are shown in Figure S18, Figure S19 and Table S6. The results indicate that the PDI-derivatives and their composite CIMs with SWCNT show self-assembly behavior on top of the active layer. The CIMs treated films exhibit more rougher surface. The root mean square (RMS) roughness of the PDIN-CNT composite CIMs surface is 6.92 nm on PM6:Y6 active layer and 10.90 nm on PM6:Y6:$PC_{71}BM$ active layer, which is slightly larger than that of the PDINO-CNT CIMs with roughness of 5.23 nm on PM6:Y6 active layer and 7.73 nm on PM6:Y6:$PC_{71}BM$ active layer.

3.4 Exciton dissociation, charge collection and recombination behavior

To investigate the impact of SWCNT composite CIMs on charge carrier recombination behavior in the OSCs, the dependences of V_{oc} and J_{sc} on light intensity (P_{light}) measurements were conducted. Figure 4(a) shows the plots of V_{oc} versus ln(P_{light}) with data fitted to $V_{oc} \propto nkT/q\ln(P_{light})$, where q is the elementary charge, k is the Boltzmann constant, and T is the Kelvin temperature, respectively [49–51]. This is the simplest and most common method to distinguish between bimolecular recombination and trap-assisted recombination. Therefore, the parameter n reflects the presence/absence of carrier traps across the active layers or at interfaces with electrodes. Trap-free carrier recombination is predicted to have a kT/q dependence on light intensity (n=1); trap assisted recombination is present if this relation shows a higher kT/q slope (n>1). Taking PDINO as an example, in the OSCs devices with bare Al electrode and Al electrode with PDINO CIM and PDINO-CNT CIM, the slopes of the fitting lines are 1.46 kT/q, 1.29 kT/q and 1.17 kT/q, respectively. It suggests that more trap assisted recombination involves under open-circuit condition in bare Al electrode than that in the PDINO-CNT/Al device, and trap-free carrier recombination (bimolecular recombination) should be the main charge recombination mechanism in the PDINO-CNT CIM device. The light-intensity dependence of J_{sc} was also measured following the formula $J_{sc} \propto (P^{\alpha}{}_{light})$, where α is related to the recombination degree, when α=1 means all free carriers are collected at the corresponding electrodes without any recombination; when α<1 indicates the existence of bimolecular recombination [49–51]. For the OSCs with PDINO-CNT CIM (Figure 4(b)), the α value is 0.976, compared to 0.949 and 0.960 for the devices without CIM and with PDINO CIM, respectively. These results verify that the PDINO-CNT CIM could sweep out charge carriers more efficiently with less slightly bimolecular recombination compared with other CIMs devices, which results in the highest PCE of 17.12% in the binary devices system.

The charge extraction properties and exciton dissociation processes were explored by the measurements of TPC, TPV and the photocurrent density (J_{ph}) versus effective bias (V_{eff}) [52–54]. As shown in Figure 4(c), TPC measurement could illustrate the charge extraction time under short-circuit conditions. For the devices with PDINO-CNT CIM, the charge extraction average time is 0.48 μs, which is obviously shorter than that of the device with bare Al electrode (0.90 μs) and with PDINO CIM (0.65 μs) under 42 mW cm^{-2} illumination. In parallel, the charge carrier lifetimes of the OSCs with different CIMs were measured by TPV measurements as shown in Figure 4(d). The result of the photovoltaic delays from the TPV can be clearly seen where the charge carrier average lifetimes of the OSCs with CNT composite CIM (7.06 μs) are significantly longer than that of the control device (3.14 μs) and PDINO device (5.48 μs). The faster charge carrier extraction and longer charge carrier lifetimes in the CNT composite CIM-based devices indicate that the CNT composite CIM could effectively help the charge extraction and exciton dissociation.

Figure 4(e) shows the J_{ph} versus V_{eff} plot of the OSCs, where J_{ph} is defined as J_L-J_D and V_{eff} is defined as V_0-V_{bias}. J_L and J_D are the photocurrent densities under illumination and in the dark condition, respectively, and V_0 is the voltage at which J_{ph}=0 and V_{bias} is the applied bias [55,56]. The charge dissociation probability ($P(E, T)$) can be calculated from the value of J_{ph} divided by the saturated photocurrent density (J_{sat}) under the short circuit conditions, where J_{sat} is the saturated J_{ph} value when $V_{eff} \geq 2$ V. The calculated $P(E, T)$ va-

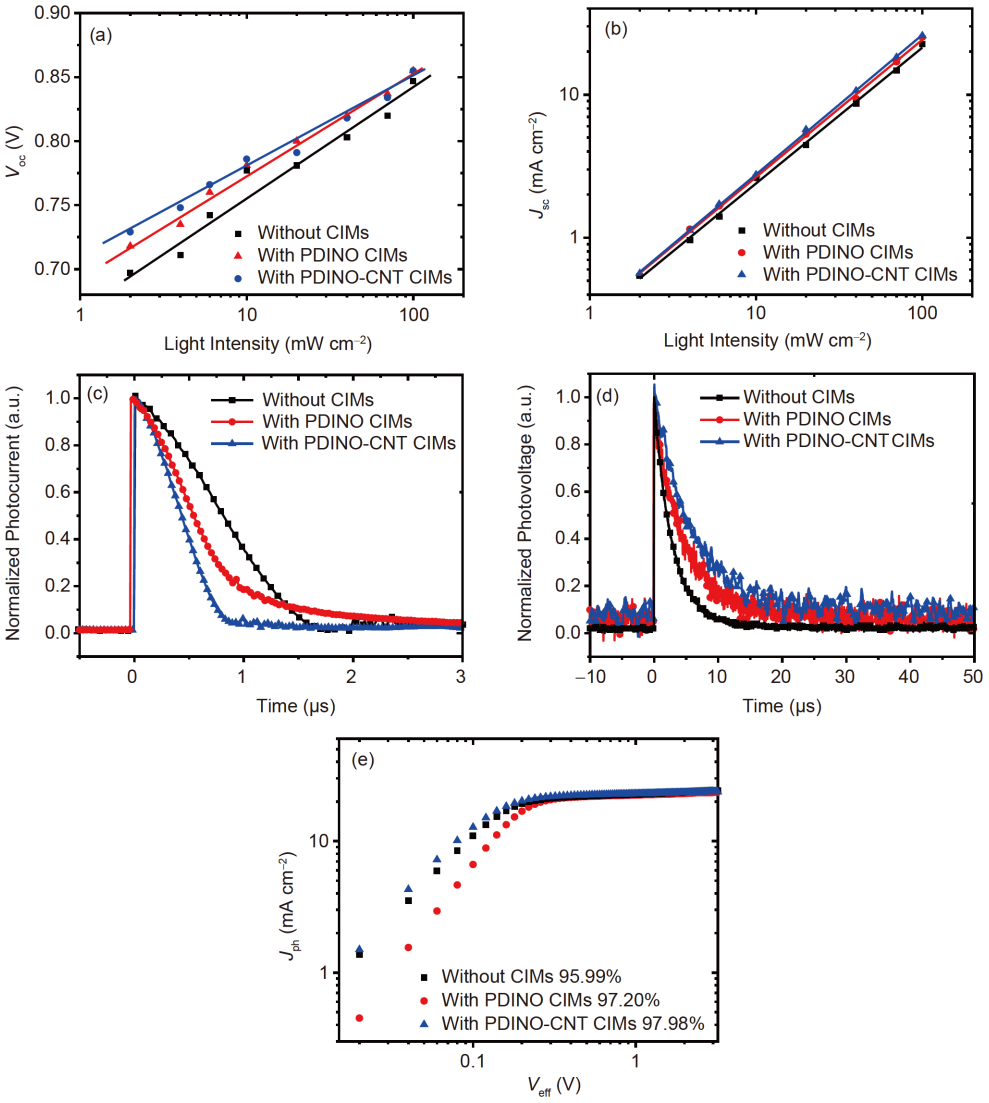

Figure 4 Dependence of (a) V_{oc} and (b) J_{sc} on light intensity (P_{light}) in the optimized OSCs based on PM6:Y6; (c) normalized transient photocurrent and (d) normalized transient photovoltage results of the devices based on PM6:Y6; (e) plots of photocurrent density (J_{ph}) *vs*. effective bias (V_{eff}) for the devices based on PM6:Y6 with different CIMs (color online).

lues are 95.99%, 97.20%, and 97.98% for the OSCs with bare Al cathode, PDINO CIM and PDINO-CNT CIM, respectively. In general, high $P(E, T)$ values represent the efficient exciton dissociation and charge collection. Therefore, this result is consistent with the TPV and TPC measurements, and the *n*-doped SWCNTs composite CIMs show the best exciton dissociation and charge collection, which could significantly improve the photovoltaic parameters including J_{sc}, FF and PCE of the OSC.

Finally, we studied the suitability of the SWCNT composite CIMs for the OSCs based on PM6:Y6 with Ag as cathode, because Ag cathode shows better stability for the *p-i-n* structured OSCs. Figure 5(a) shows *J-V* curves of the OSCs based on PM6:Y6 with Ag electrode and different CIMs under the illumination of AM 1.5 G, 100 mW cm^{-2}, and Table 3 listed the photovoltaic performance data of the corresponding OSCs. In the binary PM6:Y6 devices, the control devices with bare silver (Ag) as the cathode exhibited the poorest PCE of 11.31% with a J_{sc} of 25.72 mA cm^{-2}, a V_{oc} of 0.755 V, and an FF of 54.97%. For the OSCs with PDIN and PDINO CIMs, the PCE increased to 16.46% (V_{oc} =0.858 V, J_{sc}=25.80 mA cm^{-2} and FF=74.39%) and 15.41% (V_{oc}=0.850 V, J_{sc}=26.24 mA cm^{-2} and FF=69.11%), respectively. When PDIN-CNT and PDINO-CNT were used as the CIMs, the PCE increased to 17.07% (V_{oc}=0.862 V, J_{sc} =26.16 mA cm^{-2} and FF=75.72%) and 16.26% (V_{oc} =0.854 V, J_{sc}=26.53 mA cm^{-2} and FF=71.76%).

In addition, the shelf-stability of the OSCs with the Ag cathode was measured. The devices with PDIN-CNT and PDINO-CNT CIMs were simply encapsulated by the water and oxygen barrier films. Figure S15 shows the results of OSC device stability experiments. The PCE of the OSCs

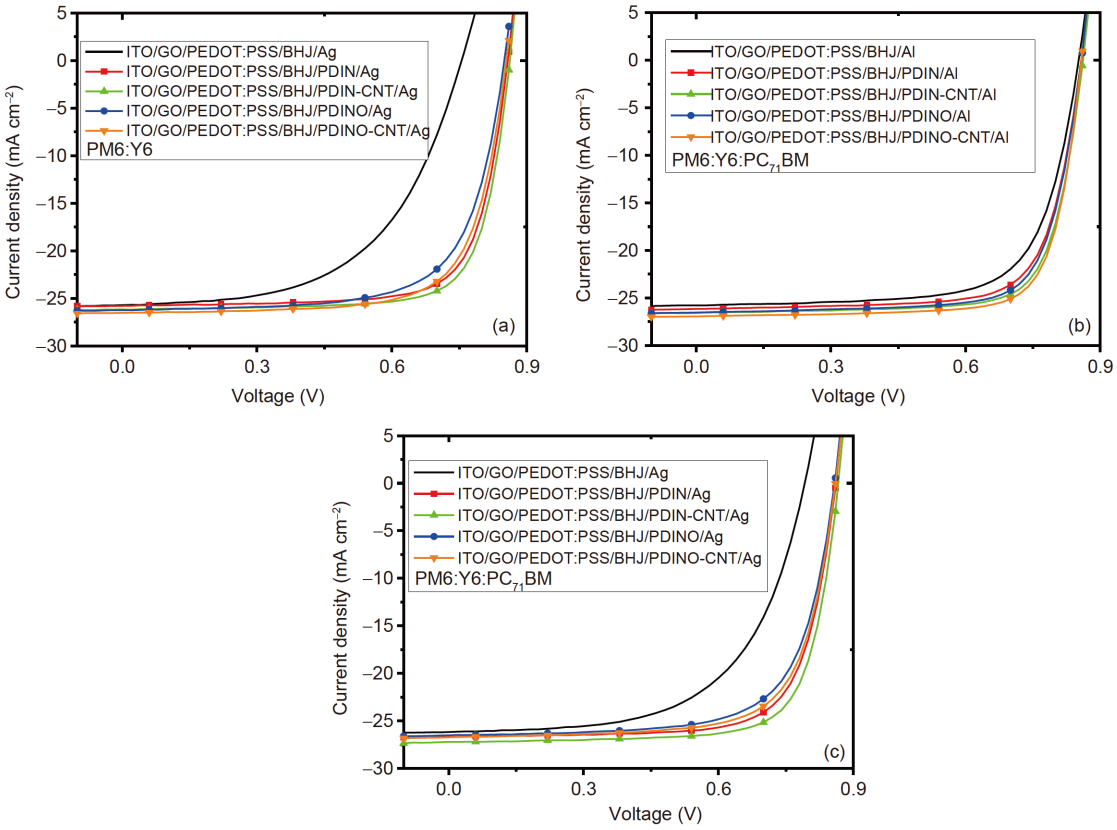

Figure 5 (a) *J-V* curves of the OSCs based on PM6:Y6 with Ag electrode and different CIMs under the illumination of AM 1.5 G, 100 mW cm^{-2}; (b) *J-V* curves of the OSCs based on PM6:Y6:$PC_{71}BM$ with Al electrode and different CIMs under the illumination of AM 1.5 G, 100 mW cm^{-2}; (c) *J-V* curves of the OSCs based on PM6:Y6:$PC_{71}BM$ with Ag electrode and different CIMs under the illumination of AM 1.5 G, 100 mW cm^{-2} (color online).

Table 3 Photovoltaic performance data of the OSCs based on PM6:Y6 with different CIMs/Ag cathode under the illumination of AM 1.5 G, 100 mW cm^{-2}

Structure of OSCs	V_{oc} (V)	J_{sc} ($J_{calc.}$)[a] (mA cm^{-2})	FF (%)	PCE_{max} (PCE_{avg}) (%)
ITO/GO/PEDOT:PSS/BHJ/Ag	0.755	25.72 (25.00)	54.97	11.31 (11.0±0.3)
ITO/GO/PEDOT:PSS/BHJ/PDIN/Ag	0.858	25.80 (25.08)	74.39	16.46 (16.2±0.3)
ITO/GO/PEDOT:PSS/BHJ/PDIN-CNT/Ag	0.862	26.16 (25.43)	75.72	17.07 (16.9±0.2)
ITO/GO/PEDOT:PSS/BHJ/PDINO/Ag	0.850	26.24 (25.51)	69.11	15.41 (15.4±0.3)
ITO/GO/PEDOT:PSS/BHJ/PDINO-CNT/Ag	0.854	26.53 (25.76)	71.76	16.26 (16.0±0.2)

a) The $J_{calc.}$ from the EQE spectrum.

with Ag cathode remained 98.14% for PDIN-CNT CIM and 91.74% for PDINO-CNT CIM, relative to their initial PCE after approximately 100 h of storage in a nitrogen atmosphere glove box. Afterward, the efficiency has almost stayed same in the following 800 h for the device with PDIN-CNT CIM (96.7%), but the PDINO-CNT CIM based device has been significantly attenuated (only 83.7%) (Figure S15). These results indicate that the devices with PDIN-CNT CIMs have better shelf-stability than that with PDINO-CNT CIMs.

3.5 Photovoltaic properties of the ternary OSCs

The ternary OSCs based on PM6:Y6:$PC_{71}BM$ were also studied for investigating the effect of the CNT-containing CIMs. The PCE of the devices with PDIN-CNT and PDINO-CNT CIMs and Al cathode improved to 17.33% (V_{oc} =0.861 V, J_{sc}= 26.59 mA cm^{-2} and FF=75.69%) and 17.70% (V_{oc}=0.858 V, J_{sc}=26.94 mA cm^{-2} and FF=76.59%), respectively (see Figure 5(b) and Table 4 and Table S7). When the Ag electrode was employed as the cathode, the PCE of the OSC with PDIN-CNT CIM is improved to 17.71% (V_{oc} =0.867 V, J_{sc}=27.20 mA cm^{-2} and FF=75.08%) (see Figure 5 (c) and Table 4), which is one of the highest values to date in the single junction OSCs. And a PCE of 17.40% (V_{oc} =0.846 V, J_{sc}=26.52 mA cm^{-2} and FF=77.60%) was certified for the device of ITO/GO/PEDOT:PSS/PM6:Y6:$PC_{71}BM$/PDIN-CNT/Ag by the National Institute of Metrology

Table 4 Photovoltaic performance data of the OSCs based on PM6:Y6:$PC_{71}BM$ with different CIMs/Al or Ag cathode under the illumination of AM 1.5 G, 100 mW cm^{-2}

Structure of OSCs	V_{oc} (V)	J_{sc} ($J_{calc.}$)[a] (mA cm^{-2})	FF (%)	PCE_{max} (PCE_{avg}) (%)
ITO/GO/PEDOT:PSS/BHJ/PDIN-CNT/Al	0.861	26.59 (25.79)	75.69	17.33 (17.0±0.3)
ITO/GO/PEDOT:PSS/BHJ/PDINO-CNT/Al	0.858	26.94 (26.13)	76.59	17.70 (17.4±0.3)
ITO/GO/PEDOT:PSS/BHJ/PDIN-CNT/Ag	0.867	27.20 (26.41)	75.08	17.71 (17.4±0.3)
ITO/GO/PEDOT:PSS/BHJ/PDINO-CNT/Ag	0.860	26.72 (25.92)	71.46	16.42 (16.1±0.3)
ITO/GO/PEDOT:PSS/BHJ/PDIN-CNT/Ag (measured in our lab by 0.030 cm^2 mask)	0.857	27.18 (26.37)	75.77	17.65
ITO/GO/PEDOT:PSS/BHJ/PDIN-CNT/Ag (certified by NIM by 0.022 cm^2 mask)	0.846	26.52	77.60	17.40

a) The $J_{calc.}$ from the EQE spectrum.

(NIM), China (see the Test Report in Figure S16, the mask area is 0.022 cm^2), very close to the value of 17.65% measured in our laboratory. The use of stable Ag cathode in the efficient OSCs indicates the potential application of the CNT-containing CIMs in the OSCs.

4 Conclusions

In conclusion, efficient CIMs PDINO-CNT and PDIN-CNT composites were obtained *via* dispersing SWCNT in classical water/alcohol soluble CIMs PDINO and PDIN. The Raman and XPS measurement results confirm the *n*-doped behavior of SWCNT by PDIN/PDINO. The *n*-doped PDI-CNT CIMs can enhance the conductivity, regulate and control the work function of cathodes, reduce the charge recombination, improve the charge extraction rate and enhance photovoltaic performance of the OSCs ultimately. High PCEs of 17.1% and 17.7% are obtained for the OSC based on PM6:Y6 and the ternary OSC based on PM6:Y6:$PC_{71}BM$, respectively, with the PDI derivatives CNT composites CIMs. The fact that the *n*-doped CNT composite CIMs work better than the graphene analogue may indicate *n*-doped nanomaterials, such as zero dimensional fullerenes, three dimensional graphenes and other two-dimensional materials are needed for further exploration for their potential applications in various optoelectronic devices.

Acknowledgements This work was supported by the National Natural Science Foundation of China (91633301, 51863002, 51973042), the Excellent Young Scientific and Technological Talents of Guizhou, China (QKHPTRC[2019]5652) and the Cultivation and Innovation of New Academic Talents of Guizhou Institute of Technology (GZLGXM-05).

Conflict of interest The authors declare no conflict of interest.

Supporting information The supporting information is available online at http://chem.scichina.com and http://link.springer.com/journal/11426. The supporting materials are published as submitted, without typesetting or editing. The responsibility for scientific accuracy and content remains entirely with the authors.

1 Yu G, Gao J, Hummelen JC, Wudl F, Heeger AJ. *Science*, 1995, 270: 1789–1791
2 Lin Y, Adilbekova B, Firdaus Y, Yengel E, Faber H, Sajjad M, Zheng X, Yarali E, Seitkhan A, Bakr OM, El-Labban A, Schwingenschlögl U, Tung V, McCulloch I, Laquai F, Anthopoulos TD. *Adv Mater*, 2019, 31: 1902965
3 Yuan J, Zhang Y, Zhou L, Zhang G, Yip HL, Lau TK, Lu X, Zhu C, Peng H, Johnson PA, Leclerc M, Cao Y, Ulanski J, Li Y, Zou Y. *Joule*, 2019, 3: 1140–1151
4 Wei Q, Liu W, Leclerc M, Yuan J, Chen H, Zou Y. *Sci China Chem*, 2020, 63: 1352–1366
5 Liu Q, Jiang Y, Jin K, Qin J, Xu J, Li W, Xiong J, Liu J, Xiao Z, Sun K, Yang S, Zhang X, Ding L. *Sci Bull*, 2020, 65: 272–275
6 Ma R, Liu T, Luo Z, Guo Q, Xiao Y, Chen Y, Li X, Luo S, Lu X, Zhang M, Li Y, Yan H. *Sci China Chem*, 2020, 63: 325–330
7 Yue D, Khatav P, You F, Darling SB. *Energy Environ Sci*, 2012, 5: 9163–9172
8 Jørgensen M, Norrman K, Gevorgyan SA, Tromholt T, Andreasen B, Krebs FC. *Adv Mater*, 2012, 24: 580–612
9 Kang H, Lee W, Oh J, Kim T, Lee C, Kim BJ. *Acc Chem Res*, 2016, 49: 2424–2434
10 Tang H, Liu Z, Hu Z, Liang Y, Huang F, Cao Y. *Sci China Chem*, 2020, 63: 802–809
11 Steim R, Kogler FR, Brabec CJ. *J Mater Chem*, 2010, 20: 2499–2512
12 Cui C, Li Y, Li Y. *Adv Energy Mater*, 2017, 7: 1601251
13 Li X, Zhang W, Usman K, Fang J. *Adv Energy Mater*, 2018, 8: 1702730
14 Hong DP, Li X, Li W, Sergei M, Aung KKK, Prashant S. *Energy Environ Sci*, 2019, 12: 1177–1209
15 Zhang J, Xue R, Xu G, Chen W, Bian GQ, Wei C, Li Y, Li Y. *Adv Funct Mater*, 2018, 28: 1705847
16 He Z, Zhong C, Huang X, Wong WY, Wu H, Chen L, Su S, Cao Y. *Adv Mater*, 2011, 23: 4636–4643
17 Wu Z, Sun C, Dong S, Jiang XF, Wu S, Wu H, Yip HL, Huang F, Cao Y. *J Am Chem Soc*, 2016, 138: 2004–2013
18 Kang Q, Ye L, Xu B, An C, Stuard SJ, Zhang S, Yao H, Ade H, Hou J. *Joule*, 2019, 3: 227–239
19 Jiao W, Ma D, Lv M, Chen W, Wang H, Zhu J, Lei M, Chen X. *J Mater Chem A*, 2014, 2: 14720–14728
20 Liu J, Zheng N, Hu Z, Wang Z, Yang X, Huang F, Cao Y. *Sci China Chem*, 2017, 60: 1136–1144
21 Wang S, Li Z, Xu X, Zhang M, Zhang G, Li Y, Peng Q. *J Mater Chem A*, 2018, 6: 22503–22507
22 Pan F, Sun C, Li Y, Tang D, Zou Y, Li X, Bai S, Wei X, Lv M, Chen X, Li Y. *Energy Environ Sci*, 2019, 12: 3400–3411
23 Pan F, Bai S, Wei X, Li Y, Tang D, Chen X, Lv M, Li Y. *Sci China Mater*, 2020, 64: 277–287
24 Miller AJ, Hatton RA, Silva SRP. *Appl Phys Lett*, 2006, 89: 133117
25 Yang Z, Chen T, He R, Guan G, Li H, Qiu L, Peng H. *Adv Mater*, 2011, 23: 5436–5439

26 Takenobu T, Takano T, Shiraishi M, Murakami Y, Ata M, Kataura H, Achiba Y, Iwasa Y. *Nat Mater*, 2003, 2: 683–688
27 Maldonado S, Morin S, Stevenson KJ. *Carbon*, 2006, 44: 1429–1437
28 Grossiord N, Loos J, Meuldijk J, Regev O, Miltner HE, Van Mele B, Koning CE. *Compos Sci Tech*, 2007, 67: 778–782
29 Zhang ZG, Qi B, Jin Z, Chi D, Qi Z, Li Y, Wang J. *Energy Environ Sci*, 2014, 7: 1966–1973
30 Lu L, Xu T, Chen W, Lee JM, Luo Z, Jung IH, Park HI, Kim SO, Yu L. *Nano Lett*, 2013, 13: 2365–2369
31 Ganji MD, Bakhshandeh A. *Commun Theor Phys*, 2013, 60: 341–347
32 Maeda Y, Kimura S, Kanda M, Hirashima Y, Hasegawa T, Wakahara T, Lian Y, Nakahodo T, Tsuchiya T, Akasaka T, Lu J, Zhang X, Yu Y, Nagase S, Kazaoui S, Minami N, Shimizu T, Tokumoto H, Saito R. *J Am Chem Soc*, 2005, 127: 10287–10290
33 Lee DY, Na SI, Kim SS. *Nanoscale*, 2016, 8: 1513–1522
34 Niu J, Yang D, Ren X, Yang Z, Liu Y, Zhu X, Zhao W, Liu SF. *Org Electron*, 2017, 48: 165–171
35 Tung VC, Kim J, Cote LJ, Huang J. *J Am Chem Soc*, 2011, 133: 9262–9265
36 Zhang M, Guo X, Ma W, Ade H, Hou J. *Adv Mater*, 2015, 27: 4655–4660
37 Zhang H, Dong H, Li Y, Jiang W, Zhen Y, Jiang L, Wang Z, Chen W, Wittmann A, Hu W. *Adv Mater*, 2016, 28: 7466–7471
38 Blom PWM, Vissenberg MCJM. *Mater Sci Eng-R-Rep*, 2000, 27: 53–94
39 Kim JS, Lägel B, Moons E, Johansson N, Baikie ID, Salaneck WR, Friend RH, Cacialli F. *Synth Met*, 2000, 111-112: 311–314
40 Davis RJ, Lloyd MT, Ferreira SR, Bruzek MJ, Watkins SE, Lindell L, Sehati P, Fahlman M, Anthony JE, Hsu JWP. *J Mater Chem*, 2011, 21: 1721–1729
41 Braun S, Salaneck WR, Fahlman M. *Adv Mater*, 2009, 21: 1450–1472
42 Zhu F, Lin X, Liu P, Jiang K, Wei Y, Wu Y, Wang J, Fan S. *Nano Res*, 2014, 7: 553–560
43 Zhou Y, Fuentes-Hernandez C, Shim J, Meyer J, Giordano AJ, Li H, Winget P, Papadopoulos T, Cheun H, Kim J, Fenoll M, Dindar A, Haske W, Najafabadi E, Khan TM, Sojoudi H, Barlow S, Graham S, Bredas JL, Marder SR, Kahn A, Kippelen B. *Science*, 2012, 336: 327–332
44 Mistry KS, Larsen BA, Bergeson JD, Barnes TM, Teeter G, Engtrakul C, Blackburn JL. *ACS Nano*, 2011, 5: 3714–3723
45 Samarajeewa DR, Dieckmann GR, Nielsen SO, Musselman IH. *Carbon*, 2013, 57: 88–98
46 Samarajeewa DR, Dieckmann GR, Nielsen SO, Musselman IH. *Nanoscale*, 2012, 4: 4544–4554
47 Wu G, Zhang ZG, Li Y, Gao C, Wang X, Chen G. *ACS Nano*, 2017, 11: 5746–5752
48 Wang H, Hsu JH, Yi SI, Kim SL, Choi K, Yang G, Yu C. *Adv Mater*, 2015, 27: 6855–6861
49 Kyaw AKK, Wang DH, Gupta V, Leong WL, Ke L, Bazan GC, Heeger AJ. *ACS Nano*, 2013, 7: 4569–4577
50 Koster LJA, Mihailetchi VD, Ramaker R, Blom PWM. *Appl Phys Lett*, 2005, 86: 123509
51 Wang J, Zhang J, Xiao Y, Xiao T, Zhu R, Yan C, Fu Y, Lu G, Lu X, Marder SR, Zhan X. *J Am Chem Soc*, 2018, 140: 9140–9147
52 Cowan SR, Street RA, Cho S, Heeger AJ. *Phys Rev B*, 2011, 83: 035205
53 Scher H, Montroll EW. *Phys Rev B*, 1975, 12: 2455–2477
54 Li Z, Gao F, Greenham NC, McNeill CR. *Adv Funct Mater*, 2011, 21: 1419–1431
55 Wu JL, Chen FC, Hsiao YS, Chien FC, Chen P, Kuo CH, Huang MH, Hsu CS. *ACS Nano*, 2011, 5: 959–967
56 Mihailetchi VD, Wildeman J, Blom PWM. *Phys Rev Lett*, 2005, 94: 126602